Geophysical Journal International

Geophys. J. Int. (2021) **225,** 1624–1636
Advance Access publication 2021 March 10
GJI Geodynamics and Tectonics

doi: 10.1093/gji/ggab051

Seismicity in the central and southeastern United States due to upper mantle heterogeneities

Arushi Saxena, Eunseo Choi, Christine A. Powell and Khurram S. Aslam

Center for Earthquake Research and Information, University of Memphis, 3890 *Central Ave, Memphis, TN* 38152*, USA. E-mail: asaxena@memphis.edu*

Accepted 2021 January 28. Received 2021 January 26; in original form 2020 January 30

SUMMARY

Sources of stress responsible for earthquakes occurring in the Central and Eastern United States (CEUS) include not only far-field plate boundary forces but also various local contributions. In this study, we model stress fields due to heterogeneities in the upper mantle beneath the CEUS including a high-velocity feature identified as a lithospheric drip in a recent regional *P*-wave tomography study. We calculate velocity and stress distributions from numerical models for instantaneous 3-D mantle flow. Our models are driven by the heterogeneous density distribution based on a temperature field converted from the tomography study. The temperature field is utilized in a composite rheology, assumed for the numerical models. We compute several geodynamic quantities with our numerical models: dynamic topography, rate of dynamic topography, gravitational potential energy (GPE), differential stress, and Coulomb stress. We find that the GPE, representative of the density anomalies in the lithosphere, is an important factor for understanding the seismicity of the CEUS. When only the upper mantle heterogeneities are included in a model, differential and Coulomb stress for the observed fault geometries in the CEUS seismic zones acts as a good indicator to predict the seismicity distribution. Our modelling results suggest that the upper mantle heterogeneities and structure below the CEUS have stress concentration effects and are likely to promote earthquake generation at preexisting faults in the region's seismic zones. Our results imply that the mantle flow due to the upper-mantle heterogeneities can cause stress perturbations, which could help explain the intraplate seismicity in this region.

Key words: Numerical modelling; Seismicity and tectonics; Seismic tomography; Cratons; Intra-plate processes.

1 INTRODUCTION

The tectonic setting of the Central and Eastern United States (CEUS) includes complex fault systems formed by two continent-scale episodes of rifting and collision (e.g. Keller *et al.* 1983; Hoffman *et al.* 1989; Thomas *et al.* 2006). Within these systems, favorably oriented faults with respect to the present-day regional or local stresses can get reactivated, generating earthquakes (e.g. Zoback 1992; Hurd & Zoback 2012). Indeed, the CEUS is characterized by several intraplate seismic zones including the New Madrid Seismic Zone (NMSZ), the Eastern Tennessee Seismic Zone (ETSZ), the South Carolina Seismic Zone (SCSZ), the Giles County Seismic Zone (GCSZ) and the Central Virginia Seismic Zone (CVSZ, Fig. 1).

Far from the tectonic plate boundaries and known to have low tectonic strain rates, earthquakes in the CEUS could be generated by local, viscous flow concentrating stress in the crust. Diverse origins of these local perturbations have been proposed, which include both crustal and lithospheric mantle heterogeneity. Kenner & Segall (2000) proposed the presence of a weaker lower crustal zone within an elastic lithosphere that acts as a local source of stress concentration. Pollitz (2001) suggested a geodynamic model for the NMSZ consisting of a sinking mafic body in the weakened lower crust that can transfer stress into an overlying, modelled elastic crust. Levandowski *et al.* (2016) showed that stress produced by a high density lower crust below the NMSZ interferes constructively with the far-field tectonic stress, causing optimal stress orientations for earthquake generation. Forte *et al.* (2007) showed that stress concentration below the NMSZ could be produced by the descent of the Farallon slab using a global geodynamic and seismic tomography based numerical model. Li *et al.* (2007) showed that lateral heterogeneities in the lithosphere could concentrate stress in the crust of the CEUS intraplate seismic zones. Chen *et al.* (2014) and Nyamwandha *et al.* (2016) independently observed a low *P*-wave velocity zone at 50–200 km depths below the NMSZ. This was interpreted as a weak zone that acts as a conduit for stress transfer into the crust. Becker *et al.* (2015) utilized a shear wave tomography model to compute temperature and density anomalies

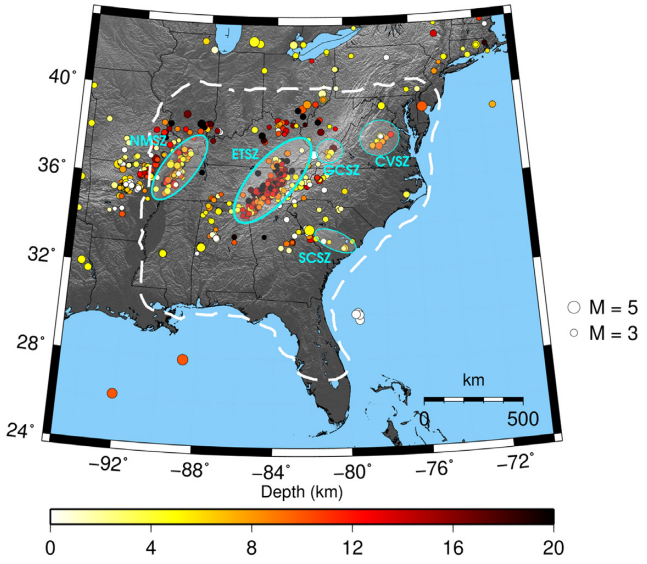

Figure 1. A shaded relief map of the study area including the central and southeastern U.S. seismic zones: New Madrid Seismic Zone (NMSZ), eastern Tennessee Seismic Zone (ETSZ) South Carolina Seismic Zone (SCSZ), Giles County Seismic Zone (GCSZ) and Central Virginia Seismic Zone (CVSZ). White dashed line represents the well-sampled region in the tomography results by Biryol *et al.* (2016) at a depth 130 km. The earthquakes that occurred over the period December 2011–December 2018 and had $M_w > 2.5$ are plotted as coloured circles. The size and colour of a circle represent the event's magnitude and depth. The earthquake catalog is obtained from the United States Geological Survey at https://earthquake.usgs.gov/earthquakes/search/, where earthquakes with $M_w > 2.5$ in the United States are published.

to set up numerical models, and found that lithospheric heterogeneity plays a crucial role in predicting the intraplate seismicity for the Western United States.

Similar considerations of crustal and mantle stress sources are yet to be made for other CEUS seismic zones such as the ETSZ, SCSZ, GCSZ and CVSZ. In a recent high-resolution *P*-wave tomography study, Biryol *et al.* (2016) found positive velocity anomalies in the upper mantle beneath the area in-between the ETSZ and the NMSZ at depths of 200–660 km, and interpreted them as foundering lithosphere. They further speculated that, since the NMSZ and the ETSZ coincide with the boundaries of lithosphere thinned by the drip, they are weakened by the underlying hot asthenosphere and thus prone to seismicity.

In this study, we investigate the effects of the upper mantle heterogeneities found in the *P*-wave tomography study by Biryol *et al.* (2016) on the seismicity in the CEUS. Using 3-D numerical models, we compute differential stress, Coulomb stress, gravitational potential energy (GPE), dynamic topography and rate of dynamic topography arising from the mantle flow generated from the heterogeneous temperature (or equivalently, density) variations converted from the tomography model. Following previous studies that have demonstrated correlation between differential stress (e.g. Baird *et al.* 2010; Zhan *et al.* 2016), deviatoric stresses (e.g. Levandowski *et al.* 2016), or topographic changes (Becker *et al.* 2015; Ghosh *et al.* 2019) with the observed intraplate seismicity, we will consider contributions of the upper mantle heterogeneity to these stress fields, GPE, dynamic topography, and rate of dynamic topography. Ghosh *et al.* (2019) took a similar approach using different lateral viscosity models, and studied how their predicted deviatoric stresses arising from long wavelength density variations in the lithosphere and the mantle, could explain the observed CEUS *P*-axes and the maximum horizontal compressive stress directions. However, Ghosh *et al.* (2019) do not consider the Coulomb failure criterion, and differs from our study in the scale of heterogeneity investigated. Ghosh *et al.* (2019) invoked lateral variations in viscosity which are dependent on the global lithospheric structure (resolved to ∼105 km), and the location of plate boundaries. In contrast, we consider short-wavelength viscosity contrasts (variations over ∼15 km) originating from the high-resolution heterogeneities in the upper mantle imaged in the Biryol *et al.* (2016) tomography model.

2 SEISMIC TOMOGRAPHY AND UPPER MANTLE HETEROGENEITIES

The tomography study by Biryol *et al.* (2016) is based on direct *P* and PKPdf (*P* wave turning in the inner core) residual travel times for IASP91 (Kennett & Engdahl 1991). The data are collected from 514 stations in the study region for 753 teleseismic earthquakes occurring between 2011 and 2015 with moment magnitude, $M_w >$ 5.5. The discretized model grid has a lateral extent of 30 km in the centre and 45 km along the boundary of the domain. The depth extent of the grid is from 36 to 915 km and consists of 21 layers, but we are only interested in the features extending down to 660 km for this study. The tomographic inversion algorithm is described in detail in the supplementary information by Biryol *et al.* (2016). Only model nodes with high quality (hit points) are used, and therefore, only model results deeper than 60 km depth are interpreted by Biryol *et al.* (2016).

Biryol *et al.* (2016) evaluate their inversion results with resolution tests. The well-sampled region in the tomographic inversion shows high-velocity anomalies with a mean amplitude of 1.9 per cent, which are interpreted as lithospheric foundering (Fig. 2a). The vertical cross-sections in Fig. 2 show that these anomalies start at ∼200 km depth with lateral dimensions of ∼2° and extend to 660 km where they widen to ∼3° (marked in Fig. 2a). According to the synthetic anomaly tests, the supposed foundering lithospheric drip with these amplitudes and dimensions should be reliably resolved.

We also assess the performance of the regional tomography model by Biryol *et al.* (2016) using global and contiguous U.S. tomography models. Fig. 2 shows the vertical cross-section along latitude 36° for four different tomography models: BNAP19 (*P*-wave tomography model of the continental U.S. concentrating on the upper mantle structure by Boyce *et al.* 2019), DNA13 (*P*-wave and *S*-wave velocity model for the contiguous United States by Porritt *et al.* 2014), NA07 (*S*-wave velocity model of the upper mantle in North America by Bedle & van der Lee 2009), and LLNL-G3Dv3 (Global *P*-wave tomography model by Simmons *et al.* 2012). The high-velocity anomalies observed by Biryol *et al.* (2016) can also be seen in the BBNAP19 and DNA13 tomography models (dashed white lines in Fig. 2). However, the colour scales in both the BBNAP19 ($\partial Vp = \pm 1$ per cent) and DNA13 ($\partial Vp = \pm 0.5$ per cent) models clearly show that the high-velocity anomaly is resolved in much higher detail ($\partial Vp = \pm 3$ per cent) in the Biryol *et al.* (2016) model. A correspondence between the Biryol *et al.* (2016) model and NA07 and LLNL-G3Dv3 models is not observed. This is understandable as NA07 is a shear wave velocity model while Biryol *et al.* (2016) utilize *P*-wave traveltimes, and LLNL-G3Dv3 is a global tomography model extending to the core–mantle boundary, which makes it difficult to resolve regional anomalies.

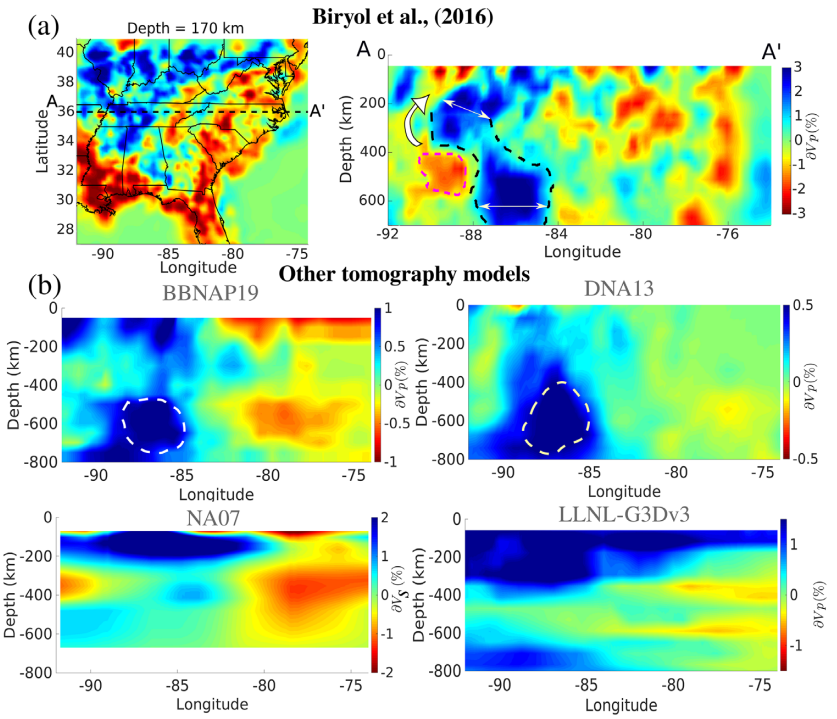

Figure 2. (a) *P*-wave tomography results by Biryol *et al.* (2016) for a layer at 170 km (left-hand panels) and a cross-section A–A′ through latitude 36° (right-hand panels). Dashed black line on the cross-section marks the approximate boundaries of the high-density anomalies interpreted as a foundering lithospheric root. Dashed magenta line indicates the low-velocity region interpreted by Biryol *et al.* (2016) as asthenospheric return flow due to the foundering lithosphere. The thick white arrow shows the direction of the return flow as speculated by Biryol *et al.* (2016) and the thin white arrows shows the lateral extent of the anomaly discussed in the text. (b) Cross-sections along 36°N of the published tomography models, BBNAP19, DNA13, NA07 and LLNL-G3Dv3. Data were retrieved from the IRIS data management centre https://ds.iris.edu/ds/products/emc/ (Trabant *et al.* 2012). See the main text for more information and references for each model. The white dashed lines in the BBNAP19 and the DNA13 models show the outline of the high-density anomaly observed in detail by Biryol *et al.* (2016).

3 MODELLING INSTANTANEOUS MANTLE FLOW

3.1 Temperature calculations

Inferring temperature from the seismic velocity anomalies has primary importance for our modelling approach because it will determine both the driving buoyancy force and the viscous resistance. We follow Cammarano *et al.* (2003)'s approach, with a few exceptions, to calculate temperatures from the seismic velocity anomalies. This approach takes into account the effects of anharmonicity (i.e. elasticity), anelasticity and the phase transition at 410 km depth. Inversion of seismic tomography to a temperature field is commonly regarded as a non-linear problem due to the shear anelasticity of seismic waves (Minster & Anderson 1981; Karato 1993; Sobolev *et al.* 1996; Goes *et al.* 2000; Artemieva *et al.* 2004) and non-linear sensitivity of elastic moduli and their pressure derivatives to temperature (Duffy & Anderson 1989; Anderson *et al.* 1992; Cammarano *et al.* 2003; Stixrude & Lithgow-Bertelloni 2005). The presence of melt or water may also introduce non-linearity in temperature effects on seismic velocities (Karato & Jung 1998) but the effects of melt and fluids are not considered in this study because of the lack of high heat flow and other substantial evidence for melting in this region of the mantle (Blackwell *et al.* 2006). Our inversion procedure is fully detailed in Appendix A.

The laterally averaged scaling of velocity anomalies to the inverted temperatures ($\partial Vp/\partial T$) is shown in Fig. 3. The non-linear sensitivity of *P*-wave velocity anomalies to temperature perturbations with depth can be seen from Fig. 3. The average $\partial Vp/\partial T$ is found to be −0.80 per cent per 100°K and −0.62 per cent per 100°K at two representative depth layers of 200 and 605 km, respectively. These values are consistent with those in Cammarano *et al.* (2003): −0.75 ± 0.15 per cent per 100°K and −0.65 per cent per 100°K at the same depths, along the mantle adiabats 1300 and 1600 °C, respectively, used in this study.

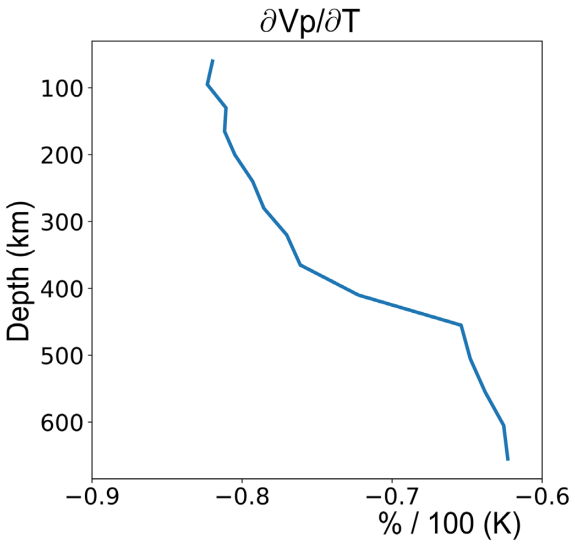

Figure 3. Depth profile of the laterally averaged *P*-wave velocity sensitivity to temperature. See text for the details of calculations.

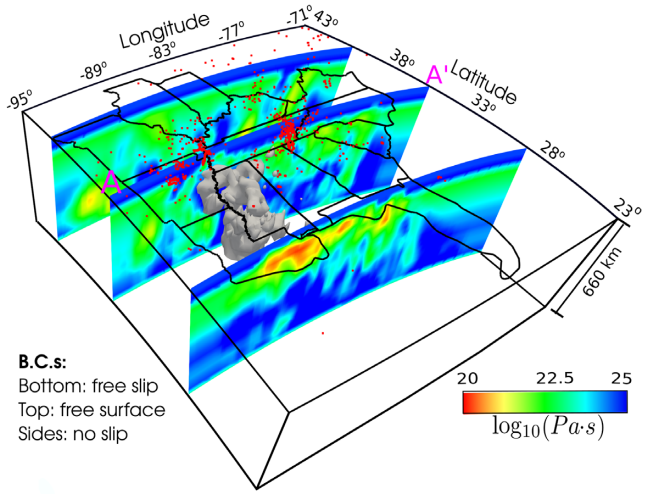

Figure 4. Model domain and cross-sections of the modelled viscosity using the temperatures based on the regional tomography by Biryol *et al.* (2016). Grey isosurface represents *P*-wave anomalies >2 per cent in the region interpreted as lithospheric foundering. The state boundaries are drawn in solid black and red dots are epicentres for the earthquake catalogue used in Fig. 1. The boundary conditions are annotated on the bottom left.

3.2 Model setup

We compute velocity and stress fields that are in equilibrium with heterogeneous buoyancy forces arising from the heterogeneous distribution of temperature-dependent density. For this calculation, we use an open-source finite element code, ASPECT version 2.0.0 (Kronbichler *et al.* 2012; Heister *et al.* 2017; Rose *et al.* 2017; Bangerth *et al.* 2018). ASPECT can solve the equations for the conservation of mass, momentum and energy using an adaptive finite element method for a variety of rock rheologies.

Our model domain is laterally bounded by longitudes, 71°W and 95.5°W and by latitudes, 23°N and 43°N. The depth range is from 0 to 660 km (Fig. 4). The domain is discretized into 0.512 million hexahedral elements with a 0.15° resolution in longitude, 0.125° in latitude and 35 km in depth. This spatial resolution is similar to that of the tomography and thus, sufficient for resolving the mantle velocity structure shown by the tomography model.

We assessed mesh resolution effects by running a model with a two times finer mesh having 2.048 million elements and found that differences in the results were small, amounting to a relative error of 2 per cent in the velocity field. All the model results presented in this study are thus based on the coarse mesh for computational efficiency. We also tested a model with an additional lateral area of 5° by 5° surrounding our domain to asses boundary effects. The overall resultant velocity and stress field are similar to those for the smaller model domain, but the magnitude of the calculated stress and velocity field at our depth of interest (15 km) near the boundaries is smaller by 10–15 per cent because the viscous effect of the same heterogeneity is now spread over a larger area. However, since the seismic zones are sufficiently far from the model domain boundaries, we show only the results for the smaller domain.

The upper mantle is typically assumed to deform by a dislocation creep at low temperatures relative to the melting temperatures of mantle rocks and by a diffusion creep at higher temperatures with respect to the melting temperatures (e.g. Gordon 1967). Our model uses a composite rheology with both dislocation and diffusion creep having different contributions depending on the temperature and pressure. In this rheology model, the effective viscosity ($\eta_{\rm eff}$) is computed as (Billen & Hirth 2007):

$$\eta_{\rm i} = \frac{1}{2} A_i^{-\frac{1}{n_i}} d^{\frac{m_i}{n_i}} \dot{\varepsilon}_i^{\frac{1-n_i}{n_i}} \exp\left(\frac{E_i + PV_i}{n_i RT}\right), \; i = \text{diff or dis}, \tag{1}$$

$$\eta_{\rm eff} = \left(\frac{1}{\eta^{\rm diff}} + \frac{1}{\eta^{\rm dis}}\right)^{-1}, \tag{2}$$

where diff and dis denote diffusion and dislocation creep, A_i is the pre-exponential factor, n_i is the power law exponent, d is the grain size, m_i is the grain size exponent, $\dot{\varepsilon}$ is the second invariant of the strain rate tensor, R is the gas constant, T is temperature obtained from the inversion of the Vp anomalies, P is pressure and E_i and V_i are the activation energy and volume, respectively. All the parameter values used in this study are given in Table 1.

It should be noted that our modelled viscosities are dependent on the temperature distribution inverted from the tomography model (described in Appendix A). The distinction between the lithospheric mantle and the sublithospheric mantle is included in our model by the temperature change with depth, and therefore, by the computed viscosities. We do not consider a crustal compositional layer because the tomography model considers only the upper mantle starting from a depth of 36 km; there are no lateral variations in the viscosity in the crust. This assumption for the crust is appropriate here, since we are interested in the effects of the lateral viscosity variations at deeper depths using differences in model outputs (HT−HM and HT−HR in Fig. 5).

The bottom boundary at 660 km has the free-slip condition (e.g. Arcay *et al.* 2007; Billen & Hirth 2007; Quinquis *et al.* 2011). For side boundaries, we tested our model with both free-slip and no-slip conditions and verified that the velocity fields at the seismic zones have the same pattern but up to 5 per cent magnitude difference in our region of interest. In this study, we only show the results for the no-slip conditions. We let the top boundary be a free surface, which was developed by Rose *et al.* (2017) in ASPECT, that can generate topography in response to the instantaneous flow in the mantle.

3.3 Geodynamic quantities

We compute three measures from our numerical model to be tested for their relevance to seismicity: GPE, dynamic topography and rate of change of dynamic topography. We also compute three stress indicators: Differential stress, Coulomb stress at observed fault geometries and optimal Coulomb stress in models isolating the effects of upper mantle heterogeneity and the foundering lithosphere. We collectively refer to these six quantities as geodynamic quantities in this study.

Molchan curves (Molchan 1990, 1991) and their associated skill (S) (Becker *et al.* 2015) are computed to quantify the earthquake prediction power of the six geodynamic quantities listed above. The predicting quantity ('predictor') is first expressed as a fraction of 'occupied' space where the predictor is less than or equal to a value in the space. This mapping implies that the maximum and the minimum value of the predictor has occupied space equal to 1 and 0, respectively. Next, we find the fraction of earthquakes that occurred outside the space occupied by the value of the predictor, referred to as the fraction of missed earthquakes. We define a Molchan curve as a plot of fractions of missed earthquakes against fractions of occupied space. When the occupied space fraction of a geodynamic quantity is 0, all the earthquakes will be missed so the fraction of missed earthquakes is 1. When the occupied space fraction is 1,

Table 1. Values of parameters for dislocation and diffusion creep.

Parameter	Symbol	Unit	Diffusion creep	Dislocation creep
Pre-exponential factor[a]	A	s^{-1}	1.5×10^{-16}	0.3×10^{-22}
Power law exponent[a]	n		1	3.5
Grain size exponent[a]	m		2	0
Activation energy[a]	E	kJ mol^{-1}	300	530
Activation volume[a]	V	cm^3 mol^{-1}	6	20
Grain size[b]	d	mm	5	5

Note: [a]Karato & Wu (1993). [b]Approximate value for olivine (Karato 1984).

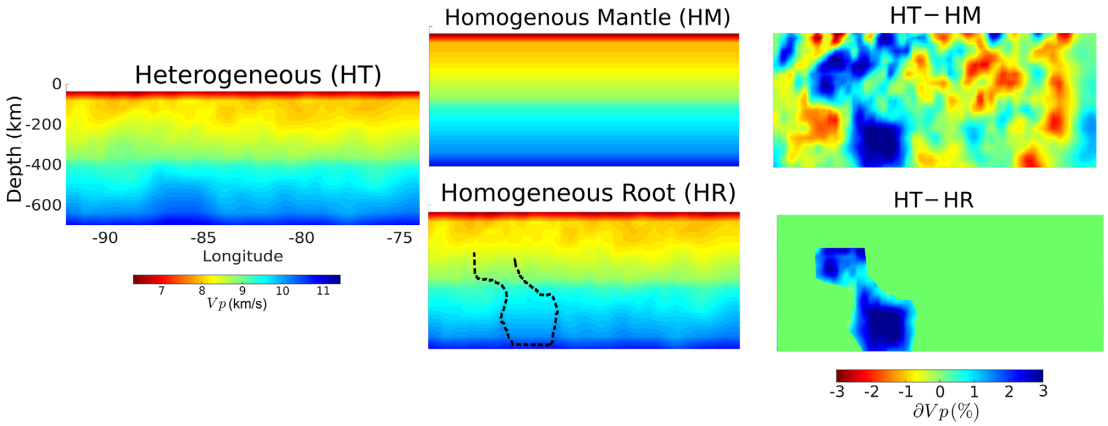

Figure 5. Cross-section along 36°N across three models: HeTerogeneous (HT), homogeneous mantle (HM) and homogeneous root (HR) models. Stress changes in HT are computed relative to HM (HT−HM) or to HT (HT−HR). HT−HM represents the effects of the whole upper mantle heterogeneity and HT−HR those of the lithospheric drip only.

the space will include all the earthquakes, making the fraction of missed earthquakes equal to 0. This implies that these curves are fixed with the boundary conditions of {0,1} and {1,0}. The skill for each predictor is computed as the area of the curve above the Molchan curve minus 0.5, such that a pure random predictor has $S = 0$, a pure correlation has $S = 0.5$, and a pure anti-correlation has $S = -0.5$. In this study, the Molchan curves are computed collectively for all the seismic zones of the CEUS (Fig. 6a).

3.3.1 *Gravitational potential energy*

We calculate GPE per unit area in our model domain (Fig. S1) following the thin-sheet approximation described in Ghosh *et al.* (2009) as:

$$\mathrm{GPE} = \int_{-h}^{L} z\rho(z)g\mathrm{d}z, \tag{3}$$

where $\rho(z)$ is the density at a depth z, g is the acceleration due to gravity taken as 9.8 $m\,s^{-2}$, h is the surface topography and L is the assumed compensation depth used as 200 km. We choose this depth to represent the approximate thickness of the lithosphere for the continents (McKenzie *et al.* 2005). Due to unavailability of the crustal structure in the tomography model by Biryol *et al.* (2016), we use the CRUST1.0 (Laske *et al.* 2013) model for crustal thickness and density distribution, and a lithospheric mantle with density distribution computed from the seismic tomography (see Appendix A for details).

3.3.2 *Dynamic topography and its rate*

The dynamic topography for our model is computed in ASPECT (Austermann *et al.* 2015). This quantity represents the radial stress at the surface due to the mantle flow generated from the buoyancy effects based on the heterogeneous temperature distribution in the model (Fig. S1). We compute the rate of dynamic topography by computing the change in dynamic topography between our instantaneous model and our model run forward in time for 10 000 yr (Becker *et al.* 2015, Fig. S1).

3.3.3 *Differential and Coulomb stress changes*

We define static Coulomb stress changes (ΔC) for a model with respect to another model as the difference in Coulomb failure function (CFF, King *et al.* 1994):

$$\Delta C = \Delta\tau - \mu'\Delta\sigma_n, \tag{4}$$

where $\Delta\tau$ and $\Delta\sigma_n$ are the difference between the models in shear (positive in the direction of slip) and normal (positive when compressive) stress, respectively, for a particular fault orientation, and μ' is the effective coefficient of friction after accounting for pore pressure. Since we do not have sufficient constraints on the effective friction coefficients (μ) for the faults in the study area, we use a value of 0.6 as done by Hurd & Zoback (2012) and Huang *et al.* (2017) for a similar study region. At lower μ, as suggested in the western United States (Townend & Zoback 2004), the faults would fail easier. Therefore, our choice of μ conservatively computes the CFF for our numerical models. CFF values are computed for the selected fault geometries based on the focal mechanisms and earthquake relocations (Table 2) at 15 km depth in all the seismic zones

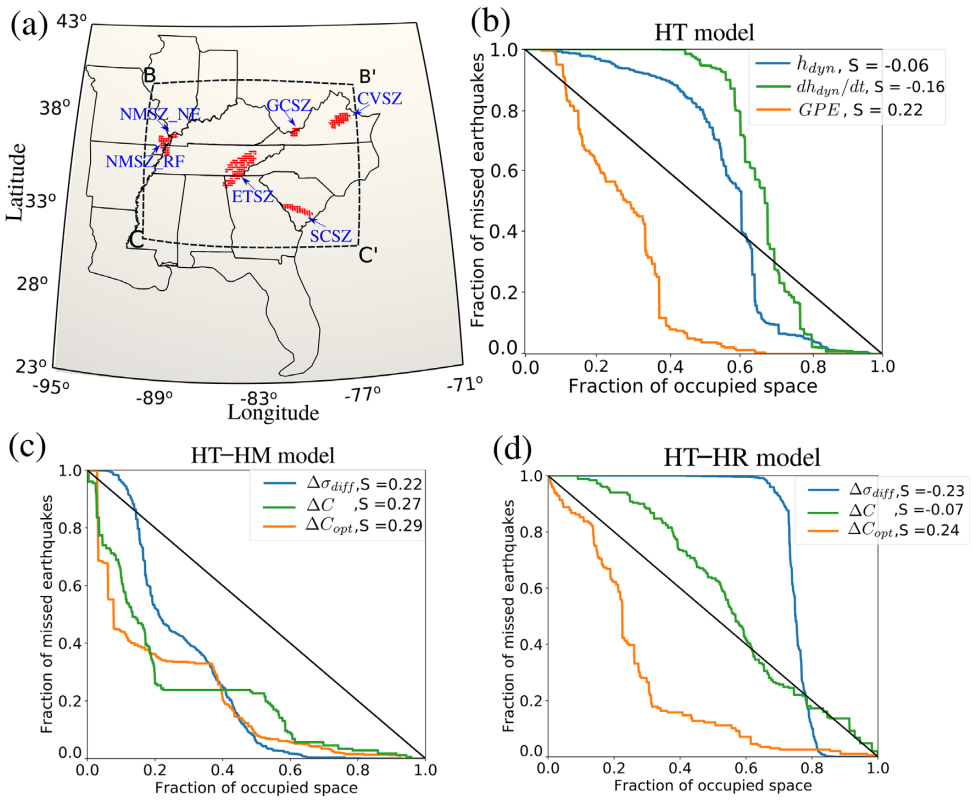

Figure 6. (a) Locations of the CEUS seismic zones plotted on the top surface of the model domain. Red dots are the nodes of the mesh that belong to the CEUS seismic zones for which the Molchan curves of Coulomb stress and the optimal Coulomb stress are computed. The box BB'CC' indicates the region for which all the other Molchan curves are calculated. (b) Molchan curves for dynamic topography ($h_{\rm dyn}$), the rate of dynamic topography change ($\mathrm{d}h_{\rm dyn}/\mathrm{d}t$) and gravitational potential energy (GPE) for the HT model. (c) Molchan curves for change in differential stress ($\Delta\sigma_{\rm diff}$), Coulomb stress change for the observed fault orientations at each seismic zone (Table 2) (ΔC) and Coulomb stress change for the optimal fault geometry where the shear stress is maximum ($\Delta C_{\rm opt}$). All are computed for HT−HM. (d) Same as (c) but for HT−HR.

Table 2. Dominant fault geometries in the CEUS seismic zones.*

Seismic zone	Strike, dip	Sense of motion	Reference
NMSZ_NE	N10°E, 90°	right-lateral	Chiu *et al.* (1992); Shumway (2008)
NMSZ_RF	N167°E, 30°SW	thrust	Csontos & Van Arsdale (2008)
ETSZ	1- N10°E, 90°; 2- E-W, 90°	right-lateral; left-lateral	Chapman *et al.* (1997); Cooley (2015); Powell & Thomas (2016)
GCSZ	E-W, 90°	left-lateral	Munsey & Bollinger (1985)
CVSZ	N30°E, 50°SE	thrust	Wu *et al.* (2015)
SCSZ	N180°E, 40°W	thrust	Chapman *et al.* (2016)

Note: *NMSZ_NE, North eastern arm of New Madrid Seismic Zone; NMSZ_RF, Reelfoot fault of the New Madrid Seismic Zone; ETSZ, Eastern Tennessee Seismic Zone; GCSZ, Giles County Seismic Zone; CVSZ, Central Virginia Seismic Zone; SCSZ, South Carolina Seismic Zone.

(Figs S3 and S4). The details of the Coulomb stress computation are in Appendix B. Differential stress, $\sigma_{\rm diff} \equiv \sigma_1 - \sigma_3$, is compared between different models with a similarly defined quantity, $\Delta\sigma_{\rm diff}$.

To facilitate comparison of models with and without the local upper-mantle heterogeneity, delineated by the velocity anomaly isosurface in Fig. 4, we denote our reference model with tomography-based temperatures plus the reference geotherm as HT (HeTerogeneous), a model with the reference geotherm in the upper mantle as HM (HoMogeneous), and a model identical with HT except that the temperature within the foundering lithosphere is replaced with the reference geotherm values as HR (Heterogeneous but having no Root). HT−HM represents the contributions from the mantle flow generated only due to the upper mantle heterogeneity (>60 km), while HT−HR shows only the contribution of the high-velocity structure interpreted as the foundering drip. Fig. 5 shows a cross-section of the tomography illustrative of these model setups. Coulomb stress changes, $\Delta C_{\rm HT-HM}$ and $\Delta C_{\rm HT-HR}$, indicate whether and how much the stress field in the model HT would promote the slip tendency of a fault relative to stress fields in HM and HR. For instance, a positive $\Delta C_{\rm HT-HM}$ for a fault geometry and a sense of motion means that the mantle heterogeneities considered in HT promote the failure of the fault relative to the laterally homogeneous mantle (HM).

3.3.4 *Optimal Coulomb stress*

We define the optimal fault orientation as the one maximizing the Coulomb stress changes of HT relative to HM ($\Delta C_{\rm HT-HM}$), and for HT relative to HR ($\Delta C_{\rm HT-HR}$). We calculate the optimal fault orientation using a grid search over strikes from N90°E to S90°E and dips from 10° to 90° at an interval of 10° for the possible senses of motion: right- and left-lateral strike-slip, normal and thrust faulting.

The optimal fault orientation could also be calculated analytically using two successive stress rotations (one to align a plane at a strike angle and then a rotation to a fault dip), and then solving for the strike and dip angles that maximize the ΔC. Since we are also interested in the ΔC distribution over the range of strikes and dips, we use the grid search method.

4 MODEL RESULTS

The Molchan curves for the geodynamic quantities, except the Coulomb stress and the optimal Coulomb stress, are computed for all the model points in the seismic zones of the CEUS: ETSZ, SCSZ, CVSZ, GCSZ and NMSZ (shown in Fig. 6a) which are contained in the well-resolved region in the Biryol *et al.* (2016) tomography. Since each seismic zone has a corresponding fault geometry, only the points within that seismic zone are accounted for when calculating the Molchan curves of the Coulomb stress and the optimal Coulomb stress (Fig. 6a).

The geodynamic quantities, GPE, $h_{\rm dyn}$ and $\mathrm{d}h_{dyn}/\mathrm{d}t$, are computed at the top surface for our reference model, which is based on the tomography converted temperatures and viscosities (HT, Fig. 5) in Fig. S1. Both the dynamic topography and its rate show negative skills for prediction of earthquakes (Fig. 6b). The skill of dynamic topography is -0.06 and that of the rate of dynamic topography is even more negative, -0.16. The GPE shows a high positive skill of $S = 0.22$.

Changes in the stress indicators, differential and Coulomb stress, for the HT−HM case are computed at a depth of 15 km (Figs S3 and S5), at which seismicity in the study area is most frequent (e.g. Mazzotti & Townend 2010). The Coulomb stress changes, ΔC, in Figs S4 and S5 are calculated for each seismic zone using the corresponding fault geometries mentioned in Table 2. These stress changes account for the effects from heterogeneities in the entire upper-mantle. Molchan curves for $\Delta\sigma_{\rm diff}$, ΔC and $\Delta C_{\rm opt}$ are shown in Fig. 6(c); and the skills of all three indicators are strongly positive: 0.22, 0.27 and 0.29, respectively.

Stress indicators computed for the HT−HR case are plotted in Figs S4 and S6 and their corresponding Molchan curves in Fig. 6(d). These stress changes represent the isolated effects of the lithospheric drip. $\Delta\sigma_{\rm diff}$ negatively correlates ($S = -0.23$) with the observed earthquake distribution. ΔC for the observed fault geometries shows minimal correlation ($S = -0.07$) with the seismicity, while $\Delta C_{\rm opt}$ shows a highly positive skill, 0.24.

5 DISCUSSION

The Molchan analyses of the geodynamic quantities for our models suggest that GPE is the best indicator of the seismicity, implying a good correlation between the seismicity and the areas of high GPE (highest skill, $S = 0.22$, in Fig. 6b). The GPE values represent the integrated vertical stress arising from the laterally varying lithospheric densities. The high GPE areas have more earthquakes because these are also the regions with thinned crust, and therefore, thicker high-density lithospheric mantle, based on the tomography model used in this study (fig. 10 in Biryol *et al.* 2016). The high predicting power of GPE suggests that the lateral density and thickness variations of the lithosphere are important factors to consider in understanding the earthquake generation in the CEUS. Although the rate of dynamic topography showed a good correlation with seismicity in the western United States (Becker *et al.* 2015), its skill in the model HT is negative, $S = -0.16$ (Fig. 6b). With $S = -0.06$, the dynamic topography itself is not a good predictor, either. This contrast in the predicting powers of vertical stress at the top surface ($h_{\rm dyn}$ and $\mathrm{d}h_{\rm dyn}/\mathrm{d}t$) and the GPE indicates that the CEUS seismic zones are better correlated with lithospheric mantle or crustal density heterogeneities than with the stresses arising due to sublithospheric mantle flow (i.e. deeper bouyancies). Although further study is needed, our finding also suggests that the rate of dynamic topography might be a useful indicator of seismicity in a rather special situation such as in the tectonically active Western United States.

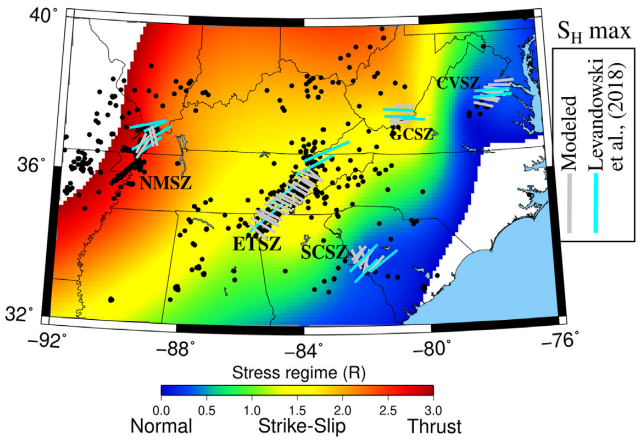

Figure 7. Maximum horizontal stress directions (S$_H$max) from the HT model (grey lines) at 15 km depth and from the focal mechanism inversion study by Levandowski *et al.* (2018) (magenta lines). The background colour map represents the stress regime parameter (R) for the model HT at 15 km depth. The white areas are the regions where R is not computed.

The overall skill associated with the stress indicators of the HT−HM model (Fig. 6c) is stronger than the HT−HR model (Fig. 6d). This is consistent with the high skill measure of the GPE in the HT model (Fig. 6b), since the total mantle density anomalies, as accounted in the HT−HM model, give rise to the GPE. Differential stress change for the HT−HM model, $\Delta\sigma_{\rm diff}^{\rm HT-HM}$, shows a positive correlation with the observed seismicity (Fig. 6c). On the other hand, the lithospheric drip alone has a negative correlation with the earthquake locations in this region (Fig. 6d). Although the positive values of differential stress changes suggest an increased potential for seismicity, even the greatest value of $\Delta\sigma_{\rm diff}^{\rm HT-HM} \sim 30$ MPa in the ETSZ (Fig. S2) is an order of magnitude less than the value required for the generation of faults at crustal depths of 10–20 km (using appropriate values for crust in Byerlee's Law). This deficiency in magnitude requires other contributions for explaining the seismicity in the CEUS like weak existing faults created during the past several Wilson cycles (Thomas *et al.* 2006) or long wavelength boundary stresses as suggested by Ghosh *et al.* (2019). From our Coulomb stress change calculations for the observed fault geometries of the seismic zones (Table 2), we find that these faults are more loaded towards failure in the heterogeneous upper mantle relative to a homogeneous upper mantle (Fig. 6c, S3). As expected from the definition of the optimal Coulomb stress ($\Delta C_{\rm opt}$), the skill for both the cases HT−HM and HT−HR at each seismic zone is maximum among all the stress indicators (Figs 6c and d).

We compare the directions of maximum horizontal stress (S$_H$max) computed from the model HT at the depth of 15 km, the depth at which most earthquakes in this region occur (Mazzotti & Townend 2010), with the S$_H$max from the study by Levandowski *et al.* (2018) (Fig. 7). These authors utilized focal mechanisms for

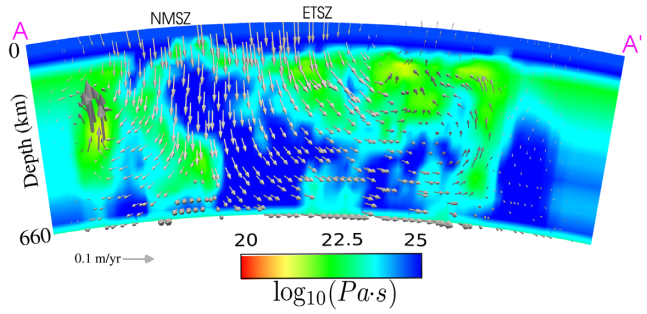

Figure 8. Velocity (arrows) and viscosity fields from the model HT on the slice AA′ (marked on Fig. 4). Large velocities observed west of the NMSZ and out of the plane correspond to the upward return flow in reaction to the downward pull of the lithospheric drip.

the contiguous United States to obtain their stresses. The $S_H$max values from our model roughly match those obtained by Levandowski *et al.* (2018) in all the seismic zones but the ETSZ (Fig. 7). The angular deviation of our modelled $S_H$max values with the inverted $S_H$max results averaged over each seismic zone considered in Fig. 7 is approximately 20°, 68°, 4°, 12° and 15° for the NMSZ, ETSZ, GCSZ, CVSZ and SCSZ, respectively. $S_H$max based on HT is NNW–SSE in the ETSZ, differing from the NE–SW direction determined using focal mechanism solutions by Levandowski *et al.* (2018) and by Mazzotti & Townend (2010). This misfit in the $S_H$max of the ETSZ has also been observed by Ghosh *et al.* (2019) (Fig. 7 of the paper) in their numerical models with lateral viscosity contrasts in the crust and the upper mantle. A possible reasoning for this misfit is stress concentration along the boundary of the strength contrast in the basement crustal rocks (Powell *et al.* 1994), which is difficult to resolve in a global tomography study used by Ghosh *et al.* (2019) or a regional mantle tomography study used here.

The distribution of stress regime parameter, *R*, (Delvaux *et al.* 1997; Simpson 1997), computed based on the model HT at 15 km depth, shows that the dominant faulting styles are thrust for the NMSZ_NE, and oblique-thrust for the GCSZ (Fig. 7). These stress regimes are consistent with the proposed faulting styles in Levandowski *et al.* (2018) for these zones, but differ from the selected studies in Table 2 which suggest strike-slip for the GCSZ and the NMSZ_NE. The HT model predicts normal faulting at the SCSZ and the CVSZ. These zones are associated with thrust faulting in Levandowski *et al.* (2018), and the studies mentioned in Table 2. This discrepancy between the modelled and predicted faulting style at the CVSZ and the SCSZ occurs because our model does not account for compressive tectonic stresses due to ridge push and long-wavelength crustal and mantle viscosity contrasts (i.e. between cratons and weak plate boundaries), which are highest at these zones due to the proximity to the plate boundary. Within the ETSZ, a strike-slip mechanism has been suggested by other studies (Chapman *et al.* 1997; Mazzotti & Townend 2010; Powell & Thomas 2016) which agrees with our model result, but differs with Cooley (2015) and Levandowski *et al.* (2018) who find normal faulting in the ETSZ. This discrepancy may be because Cooley (2015) and Levandowski *et al.* (2018) consider new focal mechanism data in their stress inversions indicating a propensity for normal faulting in the ETSZ.

A broad downward flow is found below both the NMSZ and ETSZ in the velocity field (Fig. 8) in the cross-section AA′ of the model HT (marked in Fig. 4). The descending flow induces upwellings along the edges of the model domain. The upwellings are observed at the surface as features F_1 and F_2 marked in Fig. S2. The broadly downward flow due to the lithospheric drip is not consistent with the asthenospheric upwelling that Biryol *et al.* (2016) proposed would occur as a counter-flow to the drip. However, asthenopsheric upwelling cannot be reliably rejected because the velocity field in our model depends on various parameters including the viscosity of the asthenosphere and the boundary conditions. Lower viscosity of the asthenosphere, for instance, would reduce the lateral extent of the downward drag by the lithospheric drip such that the region beneath the NMSZ might not be affected as strongly as in the current model. We ran models with only diffusion creep and only dislocation creep and found similar flow directions but a different flow law might alter the flow pattern around the high-density foundering lithosphere. A model with depth dependent viscosity with a high viscosity layer in the transition zone would inhibit a downward flow from the high-density lithospheric drip, making the velocity vectors turn at shallower depths.

Forte *et al.* (2007) presented numerical models involving viscosities based on the joint inversion of seismic and geodynamic data and observed a downward vertical flow beneath the NMSZ, that interacts with the overlying lithosphere to generate seismicity. Comparing our flow field with the results from Forte *et al.* (2007), we can see a similar vertical flow at depths of 300–500 km, but the velocity patterns at shallower depths differ significantly. A possible reason for the mismatch is the difference in the tomography studies utilized for the numerical models. Our study incorporates a regional tomography model (Biryol *et al.* 2016), while the Forte *et al.* (2007) model is a global model focusing on much larger wavelength anomalies.

This study focuses on the contribution from local stress perturbations due to the upper mantle heterogeneities on the seismicity of the CEUS. Other likely mechanisms to explain the earthquakes in this region include the presence of spatially limited weak zones activated under plate boundary stresses, and stress concentrations due to large-scale viscosity variations, such as cratons and plate boundaries. The idea of finite weaknesses under far-field stress has been studied previously by Kenner & Segall (2000) and Zhan *et al.* (2016) for the NMSZ. Kenner & Segall (2000) proposed a model with a weak lower crustal zone within an elastic lithosphere that acts as a local source of stress concentration from the far-field stresses. Similarly, based on a regional tomography model by Pollitz & Mooney (2014), Zhan *et al.* (2016) found that weak upper mantle inferred from low seismic velocities can focus stress in the NMSZ crust. Ghosh *et al.* (2019) found that large-scale lithospheric structure variations (and, therefore, viscosities) could alter the strain-rates, and affect the seismicity of the CEUS. The regional stress direction is northeast–southwest compressive stress for the CEUS (Zoback & Zoback 1989). It might be possible to superimpose the contributions from the plate boundary, large-scale stress sources, and local stress sources for a first-order understanding using a viscoplastic model that accounts for pre-existing weaknesses. However, our model is based on the upper-mantle tomography study and does not account for the spatially limited crustal weak zones (fault zones), or the stress concentration from the large-scale mantle flow. This complexity is outside the scope of this study and is not addressed further.

Time dependent modelling will be needed to address the mechanism for the origin of a foundering drip in the CEUS. It has been proposed by Biryol *et al.* (2016) that the lithospheric foundering could have started due to Rayleigh-Taylor instability associated with the presence of an eulogized root as proposed by Le Pourhiet *et al.* (2006) in the western United States. Such an investigation in this region would call for more sophisticated techniques such as

backward advection modelling (e.g. Conrad & Gurnis 2003), quasi-reversibility (Glišović & Forte 2016) or adjoint methods (e.g. Bunge *et al.* 2003; Liu *et al.* 2008) for the calculation of initial conditions on temperature, viscosity and density, which has not been done in this study.

It is also possible that the dense high-velocity mantle feature imaged by Biryol *et al.* (2016) is part of the subducted Farallon slab below this region (Schmid *et al.* 2002; Mooney & Kaban 2010; Sigloch *et al.* 2008; Schmandt & Humphreys 2010; Sigloch 2011). Schmid *et al.* (2002) used kinematic thermal modelling to track the subduction history of the Farallon slab and found that the Farallon lithosphere continues to the central United States and is still a negative thermal anomaly observable in the seismic tomography studies. Mooney & Kaban (2010) computed the gravity signal from the upper mantle for North America and observed a large gravity high in the southeastern United States, which they attributed to the east-dipping Farallon slab. Schmandt & Humphreys (2010) present *Vp* and *Vs* tomographic images for the western United States and interpret their positive velocity anomalies in the Rockies as the eastward dipping segmented Farallon slab. Sigloch *et al.* (2008); Sigloch (2011) present *P*-wave tomography for North America to a depth of 1800 km, and interpret a high-velocity anomaly in the CEUS at the mantle transition depths as a stagnant fragment of the Farallon slab. We do not comment on the origin of this high-velocity feature but follow the naming convention by Biryol *et al.* (2016) as a drip in this study. Additional observations such as low dynamic topography at the surface would be required to confirm if the high velocity is indeed attached to the lithosphere or is a remnant Farallon slab.

6 CONCLUSIONS

In this study, we advance the understanding on the role of upper mantle stress perturbations in the generation of intraplate seismicity by utilizing the highest upper mantle resolution tomography study (Biryol *et al.* 2016) to date for setting up numerical models with laterally heterogeneous viscosity and density. We also explore the isolated effects of upper-mantle heterogeneity and a positive *P*-wave velocity anomaly, interpreted by Biryol *et al.* (2016) as a lithospheric drip in our numerical models. We follow the novel Molchan analysis approach to quantify various earthquake metrics with their corresponding skills, *S*, following the work by Becker *et al.* (2015) in the Western United States. We compute earthquake predictors for our numerical models, such as the rate of creation of dynamic topography and GPE, which have not been investigated in the previous studies.

Our analysis of various earthquake predictors to understand the seismicity in the CEUS has revealed that the lateral upper-mantle heterogeneity below this region plays a significant role in increasing the differential stress ($S = 0.22$) and Coulomb stress ($S = 0.27$) at observed fault geometries. Moreover, we also find that upper mantle structural heterogeneity and density anomalies measured using GPE ($S = 0.22$) are important for understanding deformation in this region. The stress indicators for the model with only the lithospheric drip do not show correspondence with the observed seismicity pattern. Therefore, our results indicate that the upper mantle flow generated from all the upper mantle heterogeneity is essential to provide a possible mechanism for reactivation of the faults in the intraplate seismicity of the CEUS. This, in turn, helps to better associate seismic hazard with the seismic zones in the CEUS.

ACKNOWLEDGEMENTS

We thank Dr Thorsten W. Becker, Dr Attreyee Ghosh, and two anonymous reviewers for their detailed review, which has greatly improved the quality and analysis of our study. We are grateful to Dr Berk Biryol for sharing their tomography results used for modelling in this study. We also thank the Computational Infrastructure for Geodynamics (geodynamics.org) which is funded by the National Science Foundation under award EAR-0949446 and EAR-1550901 for supporting the development of ASPECT. The parameter file for the final reference model, HT and the jupyter notebook created for the inversion of seismic tomography is available at https://github.com/alarshi/ceus_seismicity.

REFERENCES

Anderson, O.L., Isaak, D. & Oda, H., 1992. High-temperature elastic constant data on minerals relevant to geophysics, *Rev. Geophys.,* **30**(1), 57–90.

Arcay, D., Tric, E. & Doin, M.-P., 2007. Slab surface temperature in subduction zones: influence of the interplate decoupling depth and upper plate thinning processes, *Earth planet. Sci. Lett.,* **255**(3–4), 324–338.

Artemieva, I.M., Billien, M., Lévêque, J.-J. & Mooney, W.D., 2004. Shear wave velocity, seismic attenuation, and thermal structure of the continental upper mantle, *Geophys. J. Int.,* **157**(2), 607–628.

Austermann, J., Pollard, D., Mitrovica, J.X., Moucha, R., Forte, A.M., DeConto, R.M. & Raymo, M.E., 2015. The impact of dynamic topography change on antarctic ice sheet stability during the mid-Pliocene warm period, *Geology,* **43**(10), 927–930.

Baird, A., McKinnon, S. & Godin, L., 2010. Relationship between structures, stress and seismicity in the Charlevoix seismic zone revealed by 3-D geomechanical models: implications for the seismotectonics of continental interiors, *J. geophys. Res.,* **115**(B11), doi:10.1029/2010JB007521.

Bangerth, W., Dannberg, J., Gassmoeller, R., Heister, T. *et al.* , 2018. ASPECT v2.0.0 [software], doi:10.5281/zenodo.1244587.

Becker, T.W., Lowry, A.R., Faccenna, C., Schmandt, B., Borsa, A. & Yu, C., 2015. Western us intermountain seismicity caused by changes in upper mantle flow, *Nature,* **524**(7566), 458–461.

Bedle, H. & van der Lee, S., 2009. S velocity variations beneath North America, *J. geophys. Res.,* **114**(B7), doi:10.1029/2008JB005949.

Billen, M.I. & Hirth, G., 2007. Rheologic controls on slab dynamics, *Geochem. Geophys. Geosyst.,* **8**(8), doi:10.1029/2007GC001597.

Biryol, C.B., Wagner, L.S., Fischer, K.M. & Hawman, R.B., 2016. Relationship between observed upper mantle structures and recent tectonic activity across the Southeastern United States, *J. geophys. Res.,* **121**(5), 3393–3414.

Blackwell, D.D., Negraru, P.T. & Richards, M.C., 2006. Assessment of the enhanced geothermal system resource base of the united states, *Nat. Resour. Res.,* **15**(4), 283–308.

Boyce, A., Bastow, I.D., Golos, E.M., Rondenay, S., Burdick, S. & Van der Hilst, R.D., 2019. Variable modification of continental lithosphere during the Proterozoic Grenville Orogeny: evidence from teleseismic P-wave tomography, *Earth planet. Sci. Lett.,* **525,** 115763.

Bunge, H.-P., Hagelberg, C. & Travis, B., 2003. Mantle circulation models with variational data assimilation: inferring past mantle flow and structure from plate motion histories and seismic tomography, *Geophys. J. Int.,* **152**(2), 280–301.

Cammarano, F., Goes, S., Vacher, P. & Giardini, D., 2003. Inferring upper-mantle temperatures from seismic velocities, *Phys. Earth planet. Inter.,* **138**(3–4), 197–222.

Chapman, M., Beale, J.N., Hardy, A.C. & Wu, Q., 2016. Modern seismicity and the fault responsible for the 1886 Charleston, South Carolina, earthquake, *Bull. seism. Soc. Am.,* **106**(2), 364–372.

Chapman, M., Powell, C., Vlahovic, G. & Sibol, M., 1997. A statistical analysis of earthquake focal mechanisms and epicenter locations in the eastern Tennessee seismic zone, *Bull. seism. Soc. Am.,* **87**(6), 1522–1536.

Chen, C., Zhao, D. & Wu, S., 2014. Crust and upper mantle structure of the New Madrid seismic zone: insight into intraplate earthquakes, *Phys. Earth planet. Inter.,* **230,** 1–14.

Chiu, J., Johnston, A. & Yang, Y., 1992. Imaging the active faults of the central New Madrid seismic zone using panda array data, *Seismol. Res. Lett.,* **63**(3), 375–393.

Conrad, C.P. & Gurnis, M., 2003. Seismic tomography, surface uplift, and the breakup of Gondwanaland: integrating mantle convection backwards in time, *Geochem. Geophys. Geosyst.,* **4**(3), doi:10.1029/2001GC000299.

Cooley, M., 2015. A new set of focal mechanisms and a geodynamic model for the eastern Tennessee seismic zone, *MS thesis*, The University of Memphis, Memphis, Tennessee, pp. 1–46.

Cottaar, S., Heister, T., Rose, I. & Unterborn, C., 2014. Burnman: a lower mantle mineral physics toolkit, *Geochem. Geophys. Geosyst.,* **15**(4), 1164–1179.

Csontos, R. & Van Arsdale, R., 2008. New Madrid seismic zone fault geometry, *Geosphere,* **4**(5), 802–813.

Delvaux, D., Moeys, R., Stapel, G., Petit, C., Levi, K., Miroshnichenko, A., Ruzhich, V. & Sankov, V., 1997. Paleostress reconstructions and geodynamics of the Baikal region, central Asia, part 2. Cenozoic rifting, *Tectonophysics,* **282**(1–4), 1–38.

Duffy, T.S. & Anderson, D.L., 1989. Seismic velocities in mantle minerals and the mineralogy of the upper mantle, *J. geophys. Res.,* **94**(B2), 1895–1912.

Dziewonski, A.M. & Anderson, D.L., 1981. Preliminary reference earth model, *Phys. Earth planet. Inter.,* **25**(4), 297–356.

Forte, A., Mitrovica, J., Moucha, R., Simmons, N. & Grand, S., 2007. Descent of the ancient Farallon slab drives localized mantle flow below the New Madrid seismic zone, *Geophys. Res. Lett.,* **34**(4), doi:10.1029/2006GL027895.

Ghosh, A., Holt, W.E. & Bahadori, A., 2019. Role of large-scale tectonic forces in intraplate earthquakes of central and eastern North America, *Geochem. Geophys. Geosyst.,* **20**(4), 2134–2156.

Ghosh, A., Holt, W.E. & Flesch, L.M., 2009. Contribution of gravitational potential energy differences to the global stress field, *Geophys. J. Int.,* **179**(2), 787–812.

Glišović, P. & Forte, A.M., 2016. A new back-and-forth iterative method for time-reversed convection modeling: implications for the Cenozoic evolution of 3-D structure and dynamics of the mantle, *J. geophys. Res.,* **121**(6), 4067–4084.

Goes, S., Govers, R. & Vacher, P., 2000. Shallow mantle temperatures under Europe from P and S wave tomography, *J. geophys. Res.,* **105**(B5), 11 153–11 169.

Goes, S. & van der Lee, S., 2002. Thermal structure of the North American uppermost mantle inferred from seismic tomography, *J. geophys. Res.,* **107**(B3), ETG–2.

Gordon, R. B., 1967. Thermally activated processes in the earth: creep and seismic attenuation, *Geophys. J. Int.,* **14** (1–4), 33–43.

Haggerty, S.E., 1995. Upper mantle mineralogy, *J. Geodyn.,* **20**(4), 331–364.

Heister, T., Dannberg, J., Gassmöller, R. & Bangerth, W., 2017. High accuracy mantle convection simulation through modern numerical methods. II: realistic models and problems, *Geophys. J. Int.,* **210**(2), 833–851.

Hoffman, P.F., Bally, A., Palmer, A., *et al.*, 1989. Precambrian geology and tectonic history of North America, in *The Geology of North America—An Overview,* pp. 447–512, eds Bally, A.W. & Palmer, A.R., Geological Society of America.

Huang, Y., Ellsworth, W.L. & Beroza, G.C., 2017. Stress drops of induced and tectonic earthquakes in the central United States are indistinguishable, *Sci. Adv.,* **3**(8), e1700772.

Hurd, O. & Zoback, M.D., 2012. Intraplate earthquakes, regional stress and fault mechanics in the central and eastern us and southeastern Canada, *Tectonophysics,* **581,** 182–192.

Karato, S., 1984. Grain-size distribution and rheology of the upper mantle, *Tectonophysics,* **104**(1–2), 155–176.

Karato, S., 1993. Importance of anelasticity in the interpretation of seismic tomography, *Geophys. Res. Lett.,* **20**(15), 1623–1626.

Karato, S. & Jung, H., 1998. Water partial melting and the origin of the seismic low velocity and high attenuation zone in the upper mantle, *Earth planet. Sci. Lett.,* **157**(3–4), 193–207.

Karato, S. & Wu, P., 1993. Rheology of the upper mantle: a synthesis, *Science,* **260**(5109), 771–778.

Katsura, T., Yoneda, A., Yamazaki, D., Yoshino, T. & Ito, E., 2010. Adiabatic temperature profile in the mantle, *Phys. Earth planet. Inter.,* **183**(1–2), 212–218.

Keller, G., Lidiak, E., Hinze, W. & Braile, L., 1983. The role of rifting in the tectonic development of the midcontinent, USA, in *Developments in Geotectonics,* Vol. **19,** pp. 391–412, Elsevier.

Kenner, S.J. & Segall, P., 2000. A mechanical model for intraplate earthquakes: application to the New Madrid seismic zone, *Science,* **289**(5488), 2329–2332.

Kennett, B. & Engdahl, E., 1991. Traveltimes for global earthquake location and phase identification, *Geophys. J. Int.,* **105**(2), 429–465.

King, G.C., Stein, R.S. & Lin, J., 1994. Static stress changes and the triggering of earthquakes, *Bull. seism. Soc. Am.,* **84**(3), 935–953.

Kronbichler, M., Heister, T. & Bangerth, W., 2012. High accuracy mantle convection simulation through modern numerical methods, *Geophys. J. Int.,* **191,** 12–29.

Laske, G., Masters, G., Ma, Z. & Pasyanos, M., 2013. Update on crust1. 0–a 1-degree global model of earth's crust, in *Proceedings of the EGU General Assembly,* 7–12 April 2013, Vienna, Austria, Geophys. Res. Abstr id. EGU2013-2658.

Le Pourhiet, L., Gurnis, M. & Saleeby, J., 2006. Mantle instability beneath the Sierra Nevada mountains in California and death valley extension, *Earth planet. Sci. Lett.,* **251**(1–2), 104–119.

Levandowski, W., Boyd, O.S. & Ramirez-Guzmán, L., 2016. Dense lower crust elevates long-term earthquake rates in the New Madrid seismic zone, *Geophys. Res. Lett.,* **43**(16), 8499–8510.

Levandowski, W., Herrmann, R.B., Briggs, R., Boyd, O. & Gold, R., 2018. An updated stress map of the continental united states reveals heterogeneous intraplate stress, *Nat. Geosci.,* **11**(6), 433.

Li, Q., Liu, M., Zhang, Q. & Sandvol, E., 2007. Stress evolution and seismicity in the central-eastern United States: insights from geodynamic modeling, *Spec. Pap.-Geol. Soc. Am.,* **425,** 149.

Liu, L., Spasojević, S. & Gurnis, M., 2008. Reconstructing Farallon plate subduction beneath North America back to the late cretaceous, *Science,* **322**(5903), 934–938.

Mazzotti, S. & Townend, J., 2010. State of stress in central and eastern North American seismic zones, *Lithosphere,* **2**(2), 76–83.

McDonough, W.F. & Rudnick, R.L., 1998. Mineralogy and composition of the upper mantle, *Rev. Mineral.,* **37,** 139–164.

McKenzie, D., Jackson, J. & Priestley, K., 2005. Thermal structure of oceanic and continental lithosphere, *Earth planet. Sci. Lett.,* **233**(3–4), 337–349.

Minster, J.B. & Anderson, D.L., 1981. A model of dislocation-controlled rheology for the mantle, *Phil. Trans. R. Soc. Lond., A,* **299**(1449), 319–356.

Molchan, G., 1990. Strategies in strong earthquake prediction, *Phys. Earth planet. Inter.,* **61**(1–2), 84–98.

Molchan, G.M., 1991. Structure of optimal strategies in earthquake prediction, *Tectonophysics,* **193**(4), 267–276.

Mooney, W.D. & Kaban, M.K., 2010. The North American upper mantle: density, composition, and evolution, *J. geophys. Res.,* **115**(B12), doi:10.1029/2010JB000866.

Munsey, J.W. & Bollinger, G., 1985. Focal mechanism analyses for Virginia earthquakes (1978-1984), *Bull. seism. Soc. Am.,* **75**(6), 1613–1636.

Nyamwandha, C.A., Powell, C.A. & Langston, C.A., 2016. A joint local and teleseismic tomography study of the Mississippi Embayment and New Madrid seismic zone, *J. geophys. Res.,* **121**(5), 3570–3585.

Pollitz, F.F., 2001. Sinking mafic body in a reactivated lower crust: a mechanism for stress concentration at the New Madrid seismic zone, *Bull. seism. Soc. Am.,* **91**(6), 1882–1897.

Pollitz, F.F. & Mooney, W.D., 2014. Seismic structure of the central us crust and shallow upper mantle: uniqueness of the Reelfoot rift, *Earth planet. Sci. Lett.,* **402,** 157–166.

Porritt, R.W., Allen, R.M. & Pollitz, F.F., 2014. Seismic imaging east of the rocky mountains with USArray, *Earth planet. Sci. Lett.,* **402,** 16–25.
Powell, C.A., Bollinger, G., Chapman, M.C., Sibol, M.S., Johnston, A.C. & Wheeler, R.L., 1994. A seismotectonic model for the 300-kilometer-long eastern tennessee seismic zone, *Science,* **264**(5159), 686–688.
Powell, C.A. & Thomas, W.A., 2016. Grenville basement structure associated with the eastern Tennessee seismic zone, southeastern USA, *Geology,* **44**(1), 39–42.
Quinquis, M.E., Buiter, S.J. & Ellis, S., 2011. The role of boundary conditions in numerical models of subduction zone dynamics, *Tectonophysics,* **497**(1–4), 57–70.
Rose, I., Buffett, B. & Heister, T., 2017. Stability and accuracy of free surface 716 time integration in viscous flows, *Phys. Earth planet. Inter.,* **262,** 90–100.
Rudnick, R.L., McDonough, W.F. & O'Connell, R.J., 1998. Thermal structure, thickness and composition of continental lithosphere, *Chem. Geol.,* **145**(3–4), 395–411.
Saxena, S.K. & Shen, G., 1992. Assessed data on heat capacity, thermal expansion, and compressibility for some oxides and silicates, *J. geophys. Res.,* **97**(B13), 19 813–19 825.
Schmandt, B. & Humphreys, E., 2010. Complex subduction and small-scale convection revealed by body-wave tomography of the western United States upper mantle, *Earth planet. Sci. Lett.,* **297**(3–4), 435–445.
Schmid, C., Goes, S., Van der Lee, S. & Giardini, D., 2002. Fate of the Cenozoic Farallon slab from a comparison of kinematic thermal modeling with tomographic images, *Earth planet. Sci. Lett.,* **204**(1–2), 17–32.
Shumway, A.M., 2008. Focal mechanisms in the northeast New Madrid seismic zone, *Seismol. Res. Lett.,* **79**(3), 469–477.
Sigloch, K., 2011. Mantle provinces under North America from multifrequency P wave tomography, *Geochem. Geophys. Geosyst.,* **12**(2), doi:10.1029/2010GC003421.
Sigloch, K., McQuarrie, N. & Nolet, G., 2008. Two-stage subduction history under North America inferred from multiple-frequency tomography, *Nat. Geosci.,* **1**(7), 458–462.
Simmons, N.A., Myers, S.C., Johannesson, G. & Matzel, E., 2012. LLNL-G3Dv3: global P wave tomography model for improved regional and teleseismic travel time prediction, *J. geophys. Res.,* **117**(B10), doi:10.1029/2012JB009525.
Simpson, R.W., 1997. Quantifying Anderson's fault types, *J. geophys. Res.,* **102**(B8), 17909–17919.
Sobolev, S.V., Zeyen, H., Stoll, G., Werling, F., Altherr, R. & Fuchs, K., 1996. Upper mantle temperatures from teleseismic tomography of french massif central including effects of composition, mineral reactions, anharmonicity, anelasticity and partial melt, *Earth planet. Sci. Lett.,* **139**(1–2), 147–163.
Stixrude, L. & Lithgow-Bertelloni, C., 2005. Thermodynamics of mantle minerals–I. Physical properties, *Geophys. J. Int.,* **162**(2), 610–632.
Thomas, W.A. *et al.*, 2006. Tectonic inheritance at a continental margin, *GSA Today,* **16**(2), 4–11.
Townend, J. & Zoback, M., 2004. Regional tectonic stress near the San Andreas fault in central and southern California, *Geophys. Res. Lett.,* **31**(15), doi:10.1029/2003GL018918.
Trabant, C., Hutko, A. R., Bahavar, M., Karstens, R., Ahern , T. & Aster , R., 2012. Data Products at the IRIS DMC: Stepping Stones for Research and Other Applications, *Seismol. Res. Lett.,* **83**(5), 846–854.
Turcotte, D. & Schubert, G., 2014. *Geodynamics,* Cambridge Univ. Press.
Watt, J.P., Davies, G.F. & O'Connell, R.J., 1976. The elastic properties of composite materials, *Rev. Geophys.,* **14**(4), 541–563.
Wu, Q., Chapman, M. & Beale, J., 2015. The aftershock sequence of the 2011 mineral, Virginia, earthquake: temporal and spatial distribution, focal mechanisms, regional stress, and theThermally activated processes in the role of coulomb stress transfer, *Bull. seism. Soc. Am.,* **105**(5), 2521–2537.
Zhan, Y., Hou, G., Kusky, T. & Gregg, P.M., 2016. Stress development in heterogenetic lithosphere: insights into earthquake processes in the New Madrid seismic zone, *Tectonophysics,* **671,** 56–62.
Zoback, M.L., 1992. Stress field constraints on intraplate seismicity in eastern North America, *J. geophys. Res.,* **97**(B8), 11 761–11 782.
Zoback, M.L. & Zoback, M.D., 1989. Tectonic stress field of the continental United States, in *Geophysical Framework of the Continental United States,* pp. 523–539, eds Pakiser, L.C. & Mooney, W.D., Geological Society of America Memoir 172, Geological Society of America.

SUPPORTING INFORMATION

Supplementary data are available at *GJI* online.

Figure S1. Computed (a) rate of dynamic topography change, (b) dynamic topography and (c) gravitational potential energy, for the HT model at the depth of 15 km. The red dots represents the earthquake epicentres.
Figure S2. (a) Differential stress changes in the HT.HM case ($\Delta\sigma$ diff) at a depth of 15 km. Black dots are earthquake epicentres from USGS data between 2011–2018. Grey lines denote the U.S. state boundaries. Seismic zones investigated in this study are the northeastern arm of the New Madrid Seismic Zone (NMSZ NE), Eastern Tennessee Seismic Zone (ETSZ), South Carolina Seismic Zone (SCSZ), Giles County Seismic Zone (GCSZ) and Central Virginia Seismic Zone (CVSZ). F1 and F2 indicates the areas of anomalously high values of $\Delta\sigma$ diff. Dashed magenta line marks the boundary of the foundering at 605 km depth. The box BB'CC' indicates HT.HR the region enlarged in subsequent figures. (b) Differential stress change for HT.HR ($\Delta\sigma$ diff) in a region centred on the ETSZ.
Figure S3. Coulomb stress change (ΔC) for HT.HM calculated for different fault orientations in Table A1) at 15 km depth. Seismic zone(s) and their corresponding optimal fault geometries are mentioned for each subplot: (a) Eastern Tennessee Seismic Zone (ETSZ) and Giles County Seismic Zone (GCSZ), left lateral vertical fault striking EW, (b) ETSZ and Northeastern arm of the New Madrid Seismic Zone (NMSZ NE) and right lateral vertical fault striking N10°E, (c) Central Virginia Seismic Zone (CVSZ) and thrust fault dipping 50°SE striking N30°E, (d) South Carolina Seismic Zone (SCSZ) and thrust fault dipping 40°W striking N–S.
Figure S4. Same as Fig. S3 but for HT-HR
Figure S5. Coulomb stress change, ΔC, for HT–HM at their optimal fault orientations. Seismic zones (magenta) and their corresponding optimal fault geometries are mentioned for each subplot.
Figure S6. Same as in Fig. S5 but for HT–HR.

Please note: Oxford University Press is not responsible for the content or functionality of any supporting materials supplied by the authors. Any queries (other than missing material) should be directed to the corresponding author for the paper.

APPENDIX A: APPENDIX: SEISMIC TOMOGRAPHY INVERSION

The effects of composition at high temperature and pressure are incorporated in seismic velocity following Cammarano *et al.* (2003) in which the elastic moduli (K, G) and densities (ρ) at reference temperature T_0 and pressure P_0 are first extrapolated at high temperatures (T) and then adiabatically at high pressures (P) following finite-strain extrapolation (Duffy & Anderson 1989). The calculations are divided at pressures 12.5 GPa to account for phase transformation of olivine to β spinel at 410 km.

To calculate density at high pressures, a mantle adiabat with potential temperature ($T_{\rm pot}$) 1300 °C was chosen for depths $\leq$410 km and 1600 °C for deeper depths up to 660 km. Strain (ϵ) is first calculated at known pressures (based on PREM model by Dziewonski & Anderson (1981)) using K_0, G_0 and their pressure derivatives,

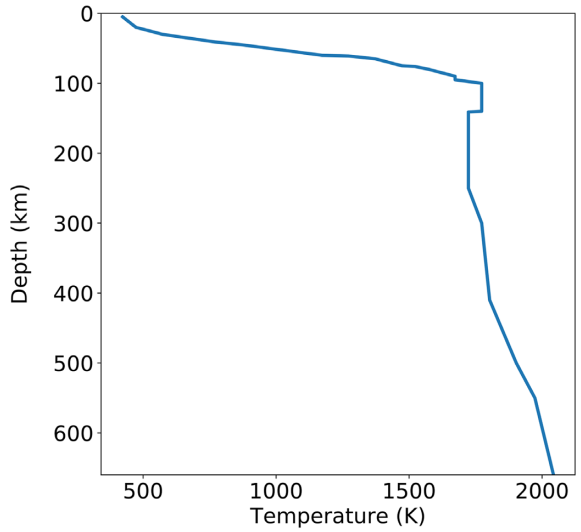

Figure A1. Depth profile of the reference temperature used, with respect to which, we compute the temperature anomalies using the input tomography model.

K'_S, G' (Table A1). Reference density calculated at the potential temperature and zero pressure $[\rho(T_{\rm pot}, P_0)]$ is then used to get the density $\rho(P, T)$.

$$P = -(1-2\epsilon)^{5/2}\left[3K_0\,\epsilon + \frac{1}{2}\left(9K_0(4-K'_S)\right)\epsilon^2\right],$$

$$\epsilon = \frac{1}{2}\left[1-\left(\frac{\rho(T,P)}{\rho(T_{\rm pot},P_0)}\right)^{2/3}\right]$$

$$\rho(T_{\rm pot}, P_0) = \rho(T_0, P_0)\,\exp\left(-\int_{T_0}^{T_{\rm pot}}\alpha(T){\rm d}T\right),$$

where thermal expansivity, $\alpha(T) = \alpha_0 + \alpha_1 T$ is truncated after the second term. Density changes due to temperature, T from the reference geotherm, $T_{\rm o}$ and pressure are calculated from above as:

$$\delta\rho = \rho(T_0, P_0)\exp\left[-\int_{T_0}^{T}\alpha(T'){\rm d}T'\right]\alpha(T))(T-T_{\rm o}). \tag{A1}$$

Temperature dependence on $K\,G$, is assumed linear while changes in K'_S, G' is calculated from the procedure in (Duffy & Anderson 1989) as:

$$\delta M|_{T,P0} = \frac{\partial M}{\partial T}(T-T_{\rm o})$$

$$\delta M'|_{T,P_0} = \left(M'(T_0)\exp\left[\int_{T_0}^{T}\alpha(T){\rm d}T\right]\alpha(T)\right)(T-T_{\rm o}),$$

where M is either K or G, δM, $\delta M'$ are changes in elastic modulus and its pressure derviate due to temperature T.

Elastic moduli changes are then evaluated at high pressures using second-order extrapolation order expansion (Duffy & Anderson 1989):

$$\delta K + \frac{4}{3}\delta G = (1-2\epsilon)^{5/2}\left[M_1 + \epsilon\left(5L_1 - 3\frac{\partial K}{\partial T}(T-T_o)\left[K' + \frac{4}{3}G'\right] - 3K_0M_2\right)\right],$$

$$\text{where, } M_1 = \delta K|_{T,P0} + \frac{4}{3}\delta G|_{T,P0};\; M_2 = \delta K'|_{T,P_0} + \frac{4}{3}\delta G'|_{T,P_0} \tag{A2}$$

The anharmonic velocity variations due to temperature and pressure are then calculated using (A1), (A2) for each mineral and then averaged using Voigt (constant strain) averaging scheme for the reference composition, discontinuous across 410 km, described in Section 3.1.

$$\delta V|_{anh} = \frac{1}{2\sqrt{K_0 + 4/3G_0}\sqrt{\rho_0}}\left[\delta K + \frac{4}{3}\delta G\right] - \frac{K_0 + 4/3G_0}{1\rho_0^{3/2}}(\delta\rho) \tag{A3}$$

Frequency dependence (anelasticity) of velocity with temperature is incorporated following Goes *et al.* (2000):

$$\delta V|_{anel} = Q_p^{-1}\frac{aH}{2RT^2\tan(\pi a/2)},$$

$$Q_p^{-1} = A\omega^a\exp\left[\frac{a(H+PV)}{RT}\right]\frac{3Vp_0^2}{4Vs_0^2} \tag{A4}$$

Here $\omega = 2\pi$, values of laboratory constants, $a = 0.15$, $A = 0.148$, activation energy $H = 500$ kJ mol^{-1}, volume $V = 20$ cm^3 mol^{-1} are taken from Sobolev *et al.* (1996). Vs_0 and Vp_0 are S- and P-wave velocities from IASP91 (Kennett & Engdahl 1991).

The reference temperature profile (T_0) for lithospheric (i.e. < 200 km) depths is the one used in (Goes & van der Lee 2002) for eastern United States and for greater depths, we follow fig. 4.56 from Turcotte & Schubert (2014) due to lack of evidence for regional geotherms at deeper depths (Fig. A1). Thermal expansivity (α) from Saxena & Shen (1992) (see Table A1). We assume a reference composition of harzburgite, that is 83 per cent olivine (ol), 15 per cent orthopyroxene (opx), 2 per cent garnet (gt) (McDonough & Rudnick 1998) for depths 40–410 km or pressure (P) <12.5 GPa. For depths from 410 to 660 km, we use a reference composition of 60 per cent Mg-wadsleyite and 40 per cent Majorite (Haggerty 1995). We use Burnman, a mineral physics toolbox (Cottaar *et al.* 2014), to calculate the mantle adiabat with a potential temperature of 1300 °C for $P < 12.5$ GPa, which is appropriate for continental lithosphere (Rudnick *et al.* 1998) and 1600° for $P > 12.5$ GPa (Katsura *et al.* 2010). Values for bulk modulus (K_S), shear modulus (G) and density (ρ) for each mineral in the composite are taken from Cammarano *et al.* (2003) and are listed in Table A1.

We account for the anelastic effects on the seismic velocity by correcting for the power law dependence of frequency on seismic attenuation, Q_p. We use linear pressure dependence on activation enthalpy [$H(P) = H_0 + VP$, V is the activation volume] in calculating Q_p [model 2 described in Sobolev *et al.* (1996)]. Another way to correct for pressure dependence on enthalpy is using melting temperature dependence [model 1 in Sobolev *et al.* (1996), i.e. $H(P) = gRT_m$ where g is constant and T_m is melting temperature]. We use model 2 because we do not include the effects of melting in the seismic anomalies for the reasons discussed earlier. We use a value of 1 Hz for the frequency in the attenuation calculation.

The inversion procedure starts with an initial guess for temperature and updates the temperature values at all the observational points in the tomography until the difference of the calculated anomalies with the observed seismic anomalies is minimized. We also calculate temperatures accounting for uncertainties in the elastic moduli and their temperature derivatives as in (Cammarano *et al.* 2003) and compare them with the results obtained here using the mean values given in Table A1. Taking the maximum values of the elastic parameters reduces the temperature sensitivity such that the negative (positive) velocity anomaly decreases (increases) temperature by a small (±90 K) magnitude. On the other hand, minimum

Table A1. Mineral physics data used in this study.[1]

Mineral	ρ (kg m^{-3})	K_S (GPa)	μ (GPa)	K'	μ'	$\partial K/\partial T$ (GPa K^{-1})	$\partial \mu/\partial T$ (GPa K^{-1})	a_0 (10^{-4})	a_1 (10^{-7})
Olivine	3222	129	81	4.2	1.4	−0.017	−0.014	0.20	0.139
Orthopyroxene	3215	109	75	7	1.6	−0.027	−0.012	0.387	0.044
Garnet	3565	171	92	4.4	1.4	−0.019	−0.01	0.099	0.116
Wadsleyite	3472	172	121	4.5	1.5	−0.014	−0.014	0.232	0.0904
Majorite	3565	171	92	4.4	1.4	−0.019	−0.01	0.0991	0.1165

Note: [1] ρ: density, K_S: adiabatic bulk modulus, μ: shear modulus, K': pressure derivative of bulk modulus, μ': pressure derivative of shear modulus, $\partial K/\partial T$: bulk modulus derivative with temperature, $\partial \mu/\partial T$: shear modulus derivative with temperature, a_0, a_1 are constants in thermal expansivity, $\alpha = a_0 + a_1 T$. Values of elastic moduli and their derivatives are from Cammarano *et al.* (2003) and thermal expansivity are from Saxena & Shen (1992).

parameter values increase the temperature sensitivity and therefore the range of temperatures obtained, by ∼180 K.

Our approach has several differences from that of Cammarano *et al.* (2003). First, we invert velocity anomalies, not absolute velocities, for temperature anomalies, which are added to an assumed reference geotherm T_o. Secondly, we use the Voigt averaging scheme to calculate elastic moduli and density of the composite rock instead of the Hashin Shtrikman scheme used by Cammarano *et al.* (2003). Although the Voigt scheme is known to overestimate the converted values (Watt *et al.* 1976), seismic velocities based on compositions averaged by the Voigt scheme, which is representative of the upper bound value for the composite (Watt *et al.* 1976), and the Reuss scheme, which is representative of the lower bound value for the composite (Watt *et al.* 1976), shows less than 0.2 per cent difference in magnitudes. Since this error is within the range of the tomography error (Biryol *et al.* 2016), we use the computationally simpler Voigt scheme. Finally, elastic moduli at high pressures are extrapolated using second-order accuracy instead of third-order for simplicity in implementation of the inversion.

APPENDIX B: APPENDIX: COULOMB STRESS CALCULATION

Stress tensors in the model outputs are given as Cartesian stress components with respect to x- and y-axes at 0° and 90° longitudes and on the equator. Stress tensors are transformed according to a rotation of the model domain by which the z-axis goes through the centre of the domain. After this rotation, x- and y-axes approximately coincide with east and north as understood in the model. Stress tensors are further transformed such that x-, y- and z-axes in the rotated Cartesian system coincide with a fault's strike, updip and normal directions (Fig. B1). We follow the convention that strike is defined as the direction that puts a dipping fault plane on the right and dip angle changes between 0° and 90°. In the final coordinate system, negative values of the shear stress on the fault plane, that is, τ_{zx} and τ_{zy} correspond to right-lateral and downdip sense of motion, respectively.

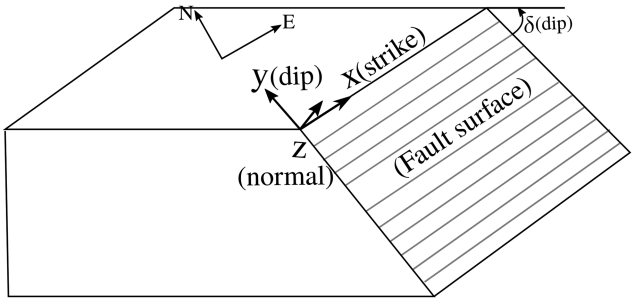

Figure B1. Cartoon sketch showing the sign convention for the strike, dip and normal to the fault surface.